Millimeter emission from protoplanetary disks : dust, cold gas, and relativistic electrons

Salter, D.M.

Table 2.3 — CN Line Measurements.

Source	CN ($2_{3/2,3/2}$–$1_{5/2,5/2}$)			CN ($2_{3/2,5/2}$–$1_{5/2,7/2}$)			CN ($2_{3/2,1/2}$–$1_{5/2,3/2}$)			Average Stats	
	υ_{LSR} [km s^{-1}]	Peak [mK]	$\int T_{mb}\,\delta\nu$ [mK km s^{-1}]	υ_{LSR} [km s^{-1}]	Peak [mK]	$\int T_{mb}\,\delta\nu$ [mK km s^{-1}]	υ_{LSR} [km s^{-1}]	Peak [mK]	$\int T_{mb}\,\delta\nu$ [mK km s^{-1}]	FWHM [km s^{-1}]	σ_{rms} [mK]
CI Tau	7.33	230	52 ± 19	6.51	76	16 ± 19	5.28	65	58 ± 35	0.42	63
CW Tau	-	-	< 94	-	-	< 94	-	-	< 94	1.00	58
CY Tau	-	-	< 97	-	-	< 97	-	-	< 97	1.00	60
DG Tau	7.63	198	171 ± 94	6.45	279	414 ± 124	5.03	294	76 ± 30	0.82	63
DN Tau	-	-	< 104	-	-	< 104	-	-	< 104	1.00	64
DO Tau	-	-	< 90	-	-	< 90	-	-	< 90	1.00	56
DQ Tau	-	-	< 98	-	-	< 98	-	-	< 98	1.00	61
DR Tau	9.65	119	56 ± 26	11.06	297	87 ± 20	11.93	110	24 ± 16	0.31	55
FT Tau	-	-	< 88	-	-	< 88	-	-	< 88	1.00	55
GO Tau	2.56	55	101 ± 41	4.07	103	37 ± 19	5.24	116	129 ± 32	1.03	42
IQ Tau	-	-	< 91	-	-	< 91	-	-	< 91	1.00	57
UZ Tau	-	-	< 79	-	-	< 79	-	-	< 79	1.00	49
V806 Tau	-	-	< 102	-	-	< 102	-	-	< 102	1.00	63

Notes. The velocities reported here are for a $\upsilon_{LSR} = 0$ centered at the theoretical frequency for the strongest hyperfine component, at 226.8747450 GHz. All reported peaks were determined from a Gaussian fit. All upper limits are given by $3 \times 1.2\,\sigma_{rms}\,\sqrt{\Delta V\,\delta\nu}$ following Jørgensen et al. (2004) where ΔV is set to 1.0 km s^{-1}.

Table 2.4 — Molecular line fluxes used to make the plots in Section 2.4 of this work.

(1) Source Name	(2) $F_{^{13}CO}$ [Jy km s^{-1}]	(3) ^{13}CO Trans.	(4) Ref.	(5) F_{HCO^+} [Jy km s^{-1}]	(6) HCO$^+$ Trans.	(7) Ref.	(8) F_{HCN} [Jy km s^{-1}]	(9) HCN Trans.	(10) Ref.	(11) F_{CN} [Jy km s^{-1}]	(12) CN Trans.	(13) Ref.
AA Tau	12.4	2–1	2	1.9	1–0	8	1.8	1–0	8	3.8	1–0	8
CI Tau	-	-	-	2.4 ± 0.7	3–2	1	< 1.6	3–2	1	2.6 ± 1.5	2–1	1
CW Tau	8.3	2–1	2	< 1.8	3–2	1	< 1.6	3–2	1	< 1.9	2–1	1
CY Tau	-	-	-	< 1.9	3–2	1	< 2.3	3–2	1	< 2.0	2–1	1
DG Tau	40.0	1–0	3	13.5 ± 1.5	3–2	1	< 0.8	3–2	1	13.7 ± 5.1	2–1	1
DL Tau	< 2.1	3–2	2	-	-	-	-	-	-	-	-	-
DM Tau	6.5	2–1	4	4.1 ± 0.5	3–2	5	2.0 ± 0.3	1–0	6	8.7 ± 0.4	2–1	6
DN Tau	14.5	2–1	2	1.2 ± 0.4	3–2	1	< 1.8	3–2	1	< 2.2	2–1	1
DO Tau	31.0	2–1	2	2.4 ± 0.5	3–2	1	< 1.4	3–2	1	< 1.9	2–1	1
DQ Tau	-	-	-	< 1.8	3–2	1	< 1.7	3–2	1	< 2.0	2–1	1
DR Tau	4.3 ± 1.2	3–2	5	3.7 ± 0.4	4–3	9	< 1.9	3–2	1	3.5 ± 1.3	2–1	1
FT Tau	-	-	-	< 1.7	3–2	1	< 1.8	3–2	1	< 1.8	2–1	1
GG Tau	5.8 ± 0.2	2–1	6	6.7 ± 0.9	3–2	6	2.8 ± 0.7	3–2	6	8.4 ± 0.4	2–1	6
GM Aur	9.3 ± 2.7	3–2	5	9.9 ± 1.2	4–3	9	-	-	-	-	-	-
GO Tau	4.1 ± 1.2	3–2	5	7.9 ± 0.8	3–2	1	< 1.5	3–2	1	5.5 ± 1.9	2–1	1
IQ Tau	-	-	-	< 2.5	3–2	1	< 1.9	3–2	1	< 1.9	2–1	1
RY Tau	4.3 ± 1.2	3–2	5	1.7 ± 0.7	4–3	9	1.6	1–0	8	0.8	1–0	8
T Tau	3.0 ± 0.2	2–1	7	3.1 ± 0.1	1–0	7	1.9 ± 0.8	2–1	10	-	-	-
UZ Tau	-	-	-	< 2.0	3–2	1	< 1.7	3–2	1	< 1.6	2–1	1
V806 Tau	-	-	-	5.8 ± 0.9	3–2	1	< 2.1	3–2	1	< 2.1	2–1	1
V892 Tau	-	-	-	-	-	-	-	-	-	-	-	-

References. 1. This work; 2. Greaves (2005); 3. Kitamura et al. (1996b); 4. Panić et al. (2008); 5. Thi et al. (2001); 6. Dutrey et al. (1997); 7. Hogerheijde et al. (1998); 8. Kessler-Silacci (2004); 9. Greaves (2004); and 10. Yun et al. (1999).
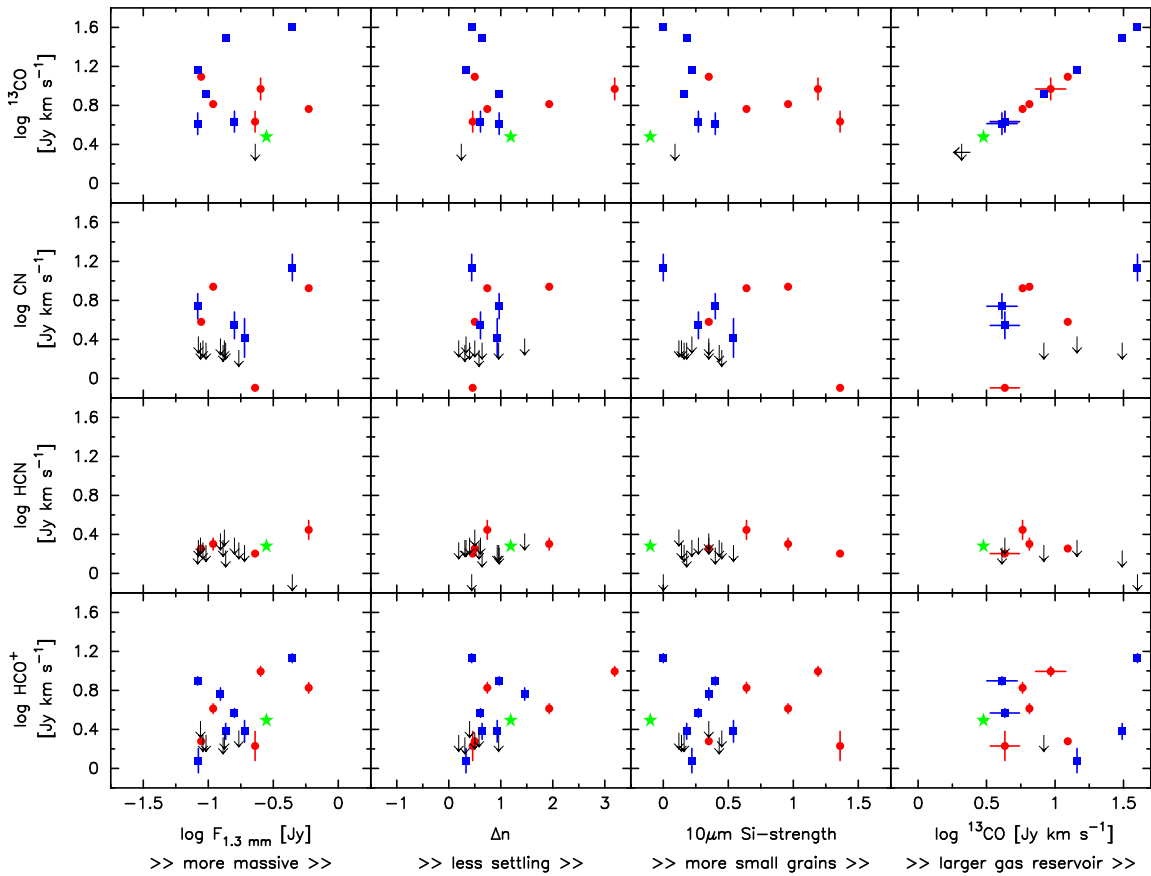
Figure 2.5 — A log plot of the integrated line intensities in Jy km s^{-1} versus several disk parameters that probe the total dust mass ($F_{1.3\,mm}$), the mid-infrared spectral slope (Δn), the 10μm silicate emission feature strength (Si-strength), and the total gas mass (inferred from the ^{13}CO line flux). Blue squares represent our JCMT observations, red circles represent data from the literature, and black arrows are used to indicate all upper limits. A green star symbol represents T Tau, whose line emission is contaminated by a large remnant envelope in the single-dish data plotted. The upper-right panel illustrates the dynamic range of the available gas reservoirs.

a factor $\geq$10 in dynamic range.

We then considered the same HCO$^+$, HCN, and CN line strengths versus $F_{1.3\,mm}$, Δn, 10μm silicate feature strength, and ^{13}CO line flux, but this time only after normalizing the line fluxes to the ^{13}CO line flux (not shown). This relation represents the line flux per unit gas mass, if we assume that the ^{13}CO line fluxes are reliable tracers of the total amount of molecular gas in each disk. No obvious trends were visible there either. Finally, we explored the equivalent plots of line flux, but then normalizing to $F_{1.3\,mm}$, or the line flux per unit dust emission. Again, no trends emerged. Together, the results show that there is no clear correlation between the observed line fluxes of HCO$^+$, HCN, or CN, and the disk dust mass, the degree of settling, the amount of small particles in the disk, or the disk gas mass. Echoing our earlier remarks, we emphasize that only detailed modeling of the emission lines can prove the presence or absence of such a correlation; but judging from the figures that plot general trends only, no strong correlation is expected from this sample.

If the molecular line flux does not depend strongly on the properties of the disk, perhaps it depends on the properties of the star. In Figure 2.6 we plot the line fluxes and upper limits against stellar mass, Hα equivalent width, bolometric luminosity, and X-ray luminosity. Similarly, we also explored the results of normalizing the line fluxes with respect to the ^{13}CO line flux and $F_{1.3\,mm}$. While the UV flux could be
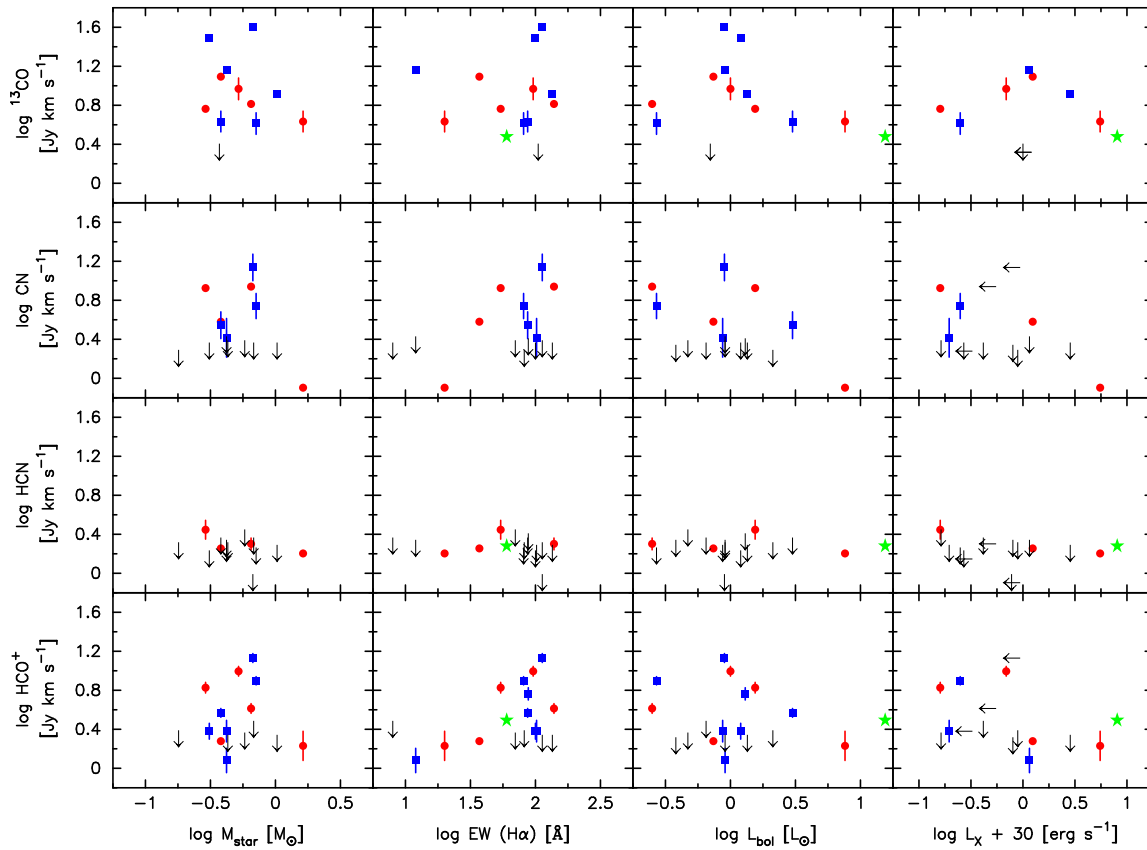
Figure 2.6 — A plot of the integrated line intensities in Jy km s⁻¹ versus several stellar parameters from the literature, including: the stellar mass ($M_\star$), the Hα equivalent width (an accretion tracer), the bolometric luminosity ($L_{\rm bol}$), and the X-ray luminosity ($L_{\rm X}$). See Figure 2.5 for an explanation of the symbols.

expected to depend strongly on the mass accretion rate, no homogeneous set of mass accretion rates is available in the literature for this sample, and these can be expected to be variable as well. Instead, we use the Hα equivalent width as a tracer and find no correlation. Indeed, no trends are apparent in any of the plots, suggesting that also such a simple connection between the stellar radiation and the emergent HCO⁺, HCN, or CN line flux is absent.

In Figure 2.7 we plot the specific relations that served as the primary motivation for this study: the ratio of CN over HCN line fluxes and the HCO⁺/¹³CO flux, respectively tracing the degree of photodissociation and the degree of ionization, versus the gas-to-dust ratio (represented by ¹³CO/$F_{1.3\,\rm mm}$) and the changing mid-infrared slope Δn, representing dust settling. As was the case for our other plots, no significant correlations are apparent. We note that the decreasing line strength with a larger gas-to-dust ratio in the upper-left panel of Figure 2.7, is the likely effect of the incorporation of the ¹³CO factor into each ratio.

In summary, we find *no* correlation between the HCO⁺, HCN, and CN line fluxes (or their ratios) and any tracer of the disk properties or those of the stellar radiation field. The line flux does not seem to be affected by any of the investigated parameters. We conclude that *the details of the input radiation field*, such as UV and Lyα strengths (Bergin et al. 2003), may be the deciding factor in the resulting line fluxes. Other contributing factors include the inner versus outer disk contributions and the temperature and density structure in the line-emitting region, both of which are discussed in Section 2.5.
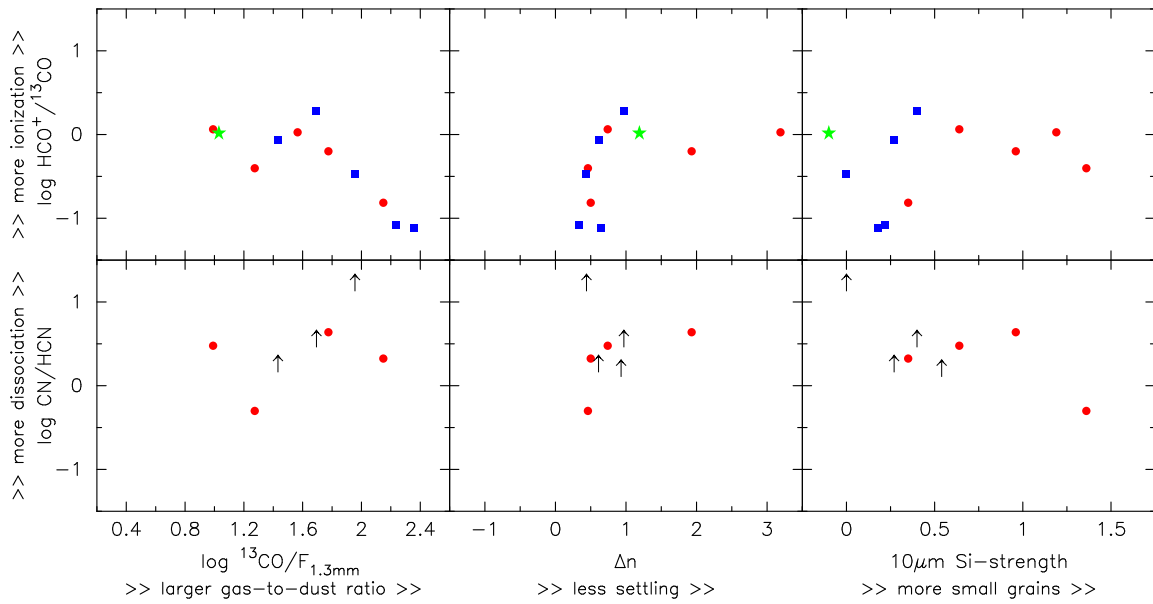
Figure 2.7 — Upper panels: The degree of ionization (traced by $HCO^+/^{13}CO$) versus the gas-to-dust ratio ($^{13}CO/F_{1.3\,mm}$), the difference in the mid-infrared spectral slope between 6, 10, and $25\mu m$ (Δn), and the strength of the $10\mu m$ silicate emission feature. Lower panels: Similar plots for the photodissociation effect (traced by CN/HCN). See Figure 2.5 for an explanation of the symbols.

2.5   Modeling the Molecular Emission

2.5.1   Disk Models

The previous section investigates the observational correlation between the measured HCO^+, HCN, and CN line intensities and upper limits, and the disk dust observables, such as millimeter continuum flux and infrared slope. While the emergent line intensity depends on the underlying molecular abundance, other factors including the disk density and temperature structure affect the emerging lines through molecular excitation and line radiative transfer. This section addresses how the modeled abundances of HCO^+, HCN, and CN (that can explain the observed emission) are related to the disk dust properties. Rather than developing an *ab initio* description of the disk structure and associated molecular chemistry, this section employs two independent models obtained from the literature (Robitaille et al. 2006; Isella et al. 2009) as starting points, and calculates the molecular abundances (assumed constant throughout the disk except in regions of freeze-out) that are consistent with our line observations.

In the first modeling approach, we make use of the online SED fitting tool[3] of Robitaille et al. (2006), the best-fit parameters of Robitaille et al. (2007), and the visual extinction values from White & Ghez (2001).[4] The continuum radiative transfer code of Whitney et al. (2003) produced the two-dimensional density and temperature structure for the best-fitting model for each source. In some cases (i.e. CI Tau, DO Tau, DR Tau, and FT Tau), the Robitaille models include remnant envelopes; these are not plotted in the figures but are included in the line calculations. However, since their H_2 number densities are $< 10^5$ cm^{-3}, the envelopes are not expected to contribute significantly to the HCO^+, HCN, or CN line emission (e.g. Hogerheijde & Sandell 2000). This first method relies entirely on spatially *unresolved* continuum data, keeping all other stellar and disk parameters free, even in cases where these properties

---

[3]Online SED fitting tool, http://caravan.astro.wisc.edu/protostars
[4]No visual extinction was included in Robitaille et al. (2007) and therefore our best-fit model may differ slightly from the one listed there.

Table 2.5 — Summary of the stellar and disk properties for the best-fitting dust models for our 13 disks.

Source	Robitaille Model						Isella Model				
	A_v [mag]	$M_\star$ [$M_\odot$]	M_d [$10^{-2} M_\odot$]	R_d [AU]	i [°]	$F_{1.3\,mm}$ [mJy]	$M_\star$ [$M_\odot$]	M_d [$10^{-2} M_\odot$]	R_d [AU]	i [°]	$F_{1.3\,mm}$ [mJy]
CI Tau	1.80 (1.80)	0.4	1.9	91	57	105	-	-	-	-	-
CW Tau	-	-	-	-	-	-	-	-	-	-	-
CY Tau	0.05 (0.03)	0.9	1.4	97	32	23	0.4	6.92	197	51	117 ± 20
DG Tau	1.60 (1.41)	1.5	3.9	158	50	254	0.3	41.7	89	18	317 ± 28
DN Tau	0.49 (0.49)	0.6	1.0	92	32	39	0.4	1.86	125	30	93 ± 8
DO Tau	4.88 (2.23)	0.8	3.2	104	57	103	-	-	-	-	-
DQ Tau	-	-	-	-	-	-	-	-	-	-	-
DR Tau	0.51 (0.51)	0.8	3.2	104	18	103	0.4	6.31	86	37	109 ± 11
FT Tau	0.00 (-)	0.2	0.8	62	50	36	-	-	-	-	-
GO Tau	-	-	-	-	-	-	0.6	7.10	670	25	57 ± 8
IQ Tau	1.44 (1.44)	1.0	3.0	101	63	74	-	-	-	-	-
UZ Tau	-	-	-	-	-	-	0.3	4.79	260	43	126 ± 12
V806 Tau	-	-	-	-	-	-	-	-	-	-	-

Notes. For the Robitaille models, the visual interstellar extinction A_v magnitudes are for the best model fit, only using the measured values from White & Ghez (2001) as an input parameter to the SED fitting tool (in parenthesis). The $M_\star$ values listed for both models are the derived values for each method. For the Isella models, the outer dust radius R_d is from Table 5 in Isella et al. (2009), defined as where the disk becomes optically thin to the stellar radiation. For UZ Tau, the Isella model in fact concerns only the spectroscopic binary component UZ Tau E. The 1.3 mm continuum fluxes ($F_{1.3\,mm}$) listed for our best-fitting Robitaille model are the SED values of the fit; and for the Isella models we list the resolved (interferometric) dust continuum measurement.

may be well known.

Our second approach uses a model by Isella et al. (2009), which explicitly takes into account the spatial distribution of the millimeter continuum emission observed with the CARMA interferometer. These authors approximate the vertical temperature structure of the disk with the two-layer description by Chiang & Goldreich (1997), and fit the grain size and opacity to resolved 1.3 mm data. In our adaptation of their models, we omit the hot surface layer because it contains insignificant amounts of molecular gas, and we extract the disk's interior temperature from Figure 7 of Isella et al. (2009). The surface density is obtained from their Equation 9 and Table 5. We then calculate the local hydrodynamic equilibrium scale height following Equations 3 and 4 from Hughes et al. (2008). We truncate the models at the transition radius, defined by Isella et al. (2009) as the location where the disk becomes optically thin to the stellar radiation (Section 2.5.3 discusses the effect of extending the disk further).

Figures 2.8 and 2.9 show the resulting temperature and density structures for our sources. For some sources, only one type of model is shown because of the availability of models in Robitaille et al. (2007) and Isella et al. (2009). Table 2.5 summarizes the parameter fits for both models. As can be immediately seen for the four sources for which both a Robitaille and an Isella model are available (i.e. CY Tau, DG Tau, DN Tau, and DR Tau), widely different disk descriptions apparently provide equally good fits to the continuum data.

The vertical height of the Robitaille models is often 4–6 times *smaller* than the Isella models. The radial extents of the disks are comparable for both approaches to within a factor of < 2. The resulting masses differ by factors of 2–10, with the Isella models always producing more massive disks. The temperature profiles of the Robtaille models are more detailed (by definition) while the Isella models at large radii are close to isothermal. In general, the temperature between the two models differs by a factor of 3–5 in the midplane. In addition to these parameters, other factors that will affect the emergent lines are the disk inclinations and stellar masses, both of which influence the widths of the lines.

To calculate the resulting molecular line emission, we populate each model disk with gas using the standard 100:1 gas-to-dust ratio, a mean molecular weight of 4.008×10^{-24} g, and constant H_2 relative abundances of 1×10^{-9} for HCO^+, 2×10^{-11} for HCN, and 1×10^{-9} for CN, based on the fractional values in the warm molecular layer for the theoretical models of Aikawa et al. (2002) and van Zadelhoff et al. (2003). In regions where the dust temperature (assumed equal to the gas temperature) drops below the CO ice evaporation temperature of 20 K, these abundances are reduced by a factor 10^3 to account for CO freeze-out. When the H_2 number density drops below 10^{-3} cm^{-3}, the molecular abundances are set to zero, effectively defining the disk edge.

The gas kinematics follow a cylindrical Keplerian velocity field with stellar masses corresponding to each model fit, as indicated in Table 2.5. A Doppler broadening factor of 0.15 km s^{-1} is also factored into the line calculations. The statistical equilibrium molecular excitation and line radiative transfer was solved using the RATRAN code (Hogerheijde & van der Tak 2000), and the emerging line emission was convolved with the appropriate Gaussian beams. The resulting line profiles are plotted alongside the disk models in Figures 2.8 and 2.9.

2.5.2 Comparison of Fixed-abundance Models

As is immediately obvious from Figures 2.8 and 2.9, the models have difficulty reproducing the detected emission lines. In four cases (CI Tau, DG Tau, DN Tau, and DO Tau) the models predict lines that are weaker than observed; in two cases (GO Tau and UZ Tau), the models predict lines that are stronger than the detected line (for GO Tau) or the obtained upper limits (for UZ Tau). In the remaining four cases (CY Tau, DR Tau, FT Tau, and IQ Tau), the predicted lines are consistent with the achieved upper limits, although for CY Tau the Isella model produces an HCO^+ line that violates the upper limit.
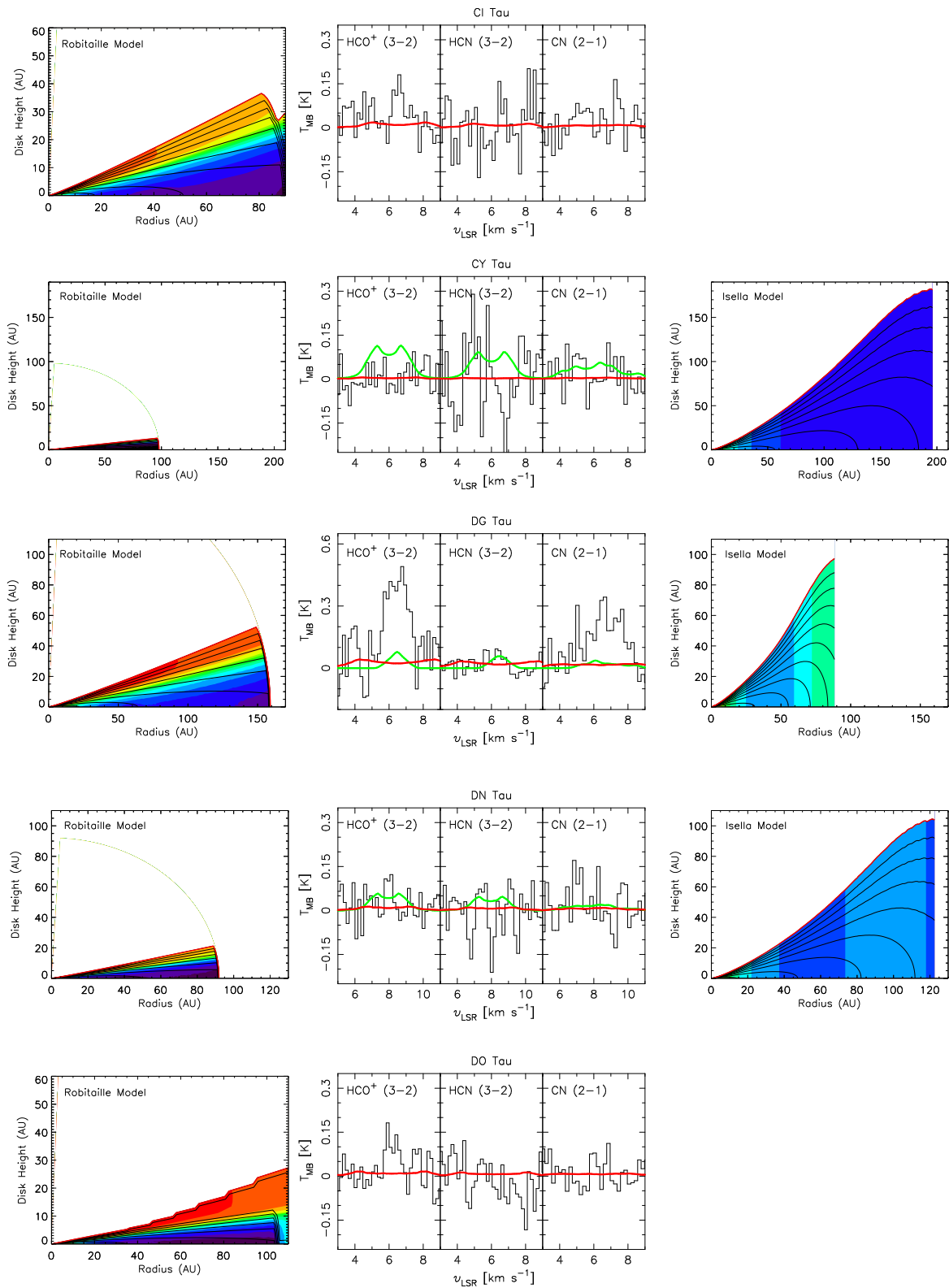
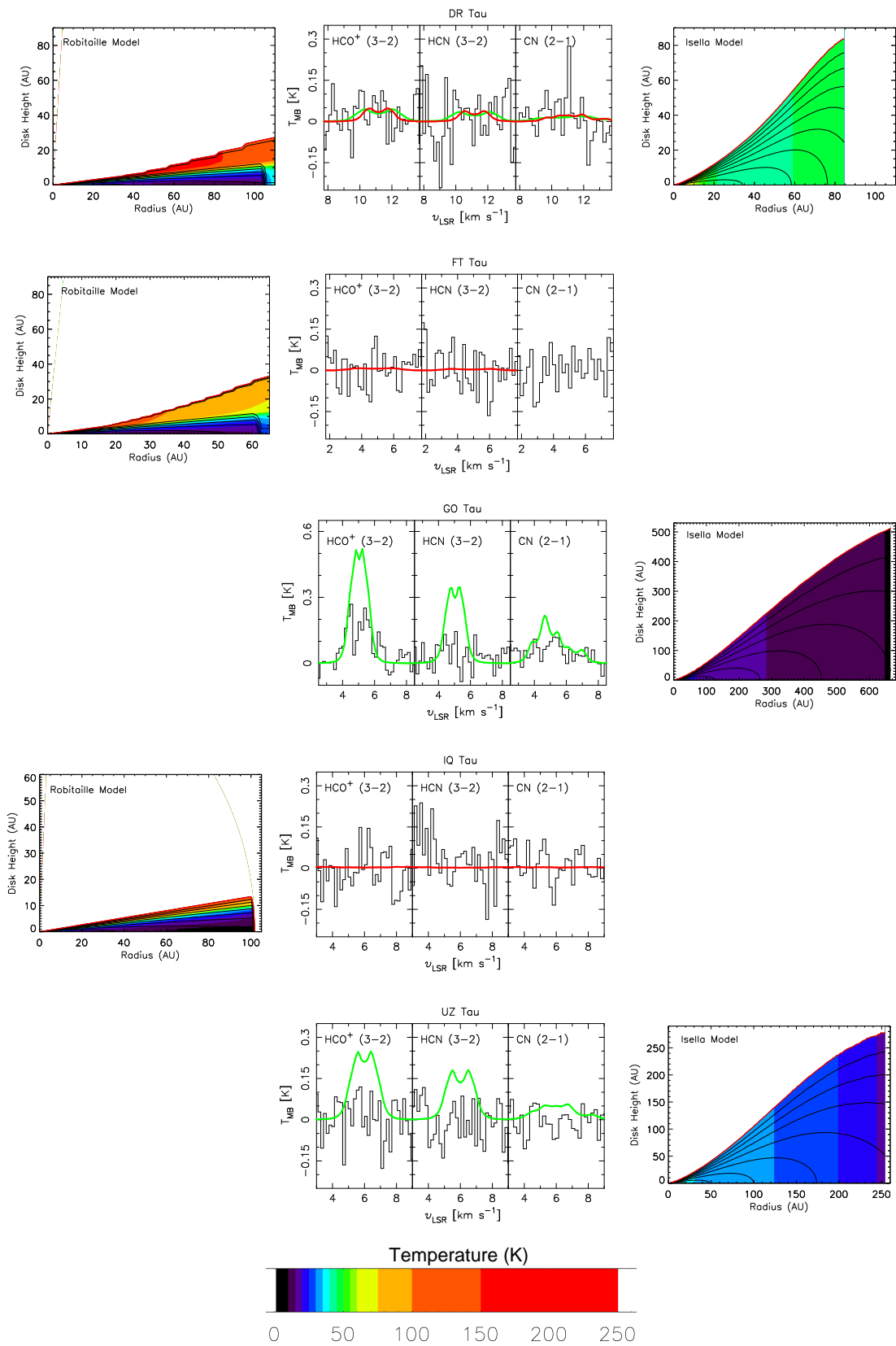**Figure 2.8 —** *See caption at the top of page 50.*

Figure 2.9 — *See caption at the top of page 50.*

Figure 2.8 Caption. Results of the general analysis. From left to right: the Robitaille disk structure; the line predictions for HCO$^+$, HCN, and CN (in red for the Robitaille model, green for the Isella model); and the Isella disk structure. The sources shown from top to bottom are: CI Tau, CY Tau, DG Tau, DN Tau, and DO Tau. For the disk structures, filled contours correspond to the temperature (in K) profile. The temperature levels are identical for all disks, designated at: 10, 15, 20, 25, 30, 35, 40, 45, 50, 55, 60, 75, 100, 150, and 250 K. A color bar is provided in Figure 2.9. The contour lines indicate the log H$_2$ number density (in cm^{-3}), indicated at whole number integrals from 3 (disk surface/edge) to 12 (typical midplane density).

Figure 2.9 Caption. Continued from Figure 2.8. The sources shown (top to bottom) are: DR Tau, GO Tau, FT Tau, GO Tau, and IQ Tau. A color bar is provided here for the filled temperature contours and applies to all disks.

Where both a Robitaille model and an Isella model are available, the Isella model always produces lines that are stronger and narrower than those of the Robitaille models. The larger stellar masses, by factors 2–5, of the latter, and the larger disk masses of the former, by factors 2–10, contribute to this difference. Inclination also plays a significant role, with more face-on orientations leading to stronger lines (cf. DO Tau and DR Tau, which are fit with the same Robitaille disk structure, but have respective inclinations of $i = 57°$ and $i = 18°$; DR Tau has predicted lines stronger by a factor of $\sim$3). Interestingly, of the six sources from our sample modeled by Isella et al. (2009), the three with *detected* line emission have $i \leq 30°$ (DG Tau, DN Tau, and GO Tau), while the sources with $i > 30°$ (CY Tau, DR Tau, and UZ Tau) are undetected (all have similar $M_\star$). Perhaps the narrower line profiles have helped to make these sources detectable.

Given the general mismatch between the predicted line intensities and widths, and the observations, it is not possible to draw conclusions about the HCO$^+$, HCN, or CN abundances this way. Simply scaling up or down the abundance will not result in a match (to the line shape); only for GO Tau do the abundances appear to lie within a factor of a few above the true values. Furthermore, as illustrated by the case of DR Tau, two *different* disk models (but with more comparable M_d, R_d, and $F_{1.3\,mm}$ values) produce very similar lines. These degeneracies make it difficult to derive reliable conclusions about the HCO$^+$, HCN, and CN abundances. Instead, more detailed modeling of individual sources may be required.

2.5.3   The Specific Case of DG Tau

Of all the sources in our sample, DG Tau offers the best case to obtain a detailed model. Its 1.3 mm continuum is brighter by a factor ≥ 2.5 than any of the other sources and it emits the strongest HCO$^+$ and CN lines. An extensive literature also exists on DG Tau describing sub-millimeter single-dish (Schuster et al. 1993; Mitchell et al. 1994) and interferometer data (Kitamura et al. 1996a,b; Dutrey et al. 1996; Testi et al. 2002; Isella et al. 2009). Its millimeter continuum emission is compact with $\sim$80% originating from within 95 AU (Isella et al. 2009). The best-fit Robitaille model obtained in the previous section (see Table 2.5, model number 3017659) matches other literature estimates of the DG Tau disk parameters (Table 2.6). Only the disk mass ($M_d = 0.042\,M_\odot$) is significantly larger than the literature values (0.015–0.025 $M_\odot$); aside from the 10$\times$ greater Isella value of 0.4 $M_\odot$. The Isella model, on the other hand, overestimates the stellar mass ($M_\star = 1.5\,M_\odot$), while literature values for $M_\star$ range from 0.3 to 0.8 $M_\odot$ and the Robitaille model yields 0.3 $M_\odot$. To model DG Tau we settle on a central stellar mass of 0.8 $M_\odot$, which is on the high end of the literature values for this object but provides the best fit to the line profiles, as discussed below.

Figure 2.10 reproduces the ^{12}CO (6–5), ^{13}CO (1–0), and C^{18}O (2–1) line observations of Schuster et al. (1993) and Kitamura et al. (1996a). The bright CO isotopologues suggest a significant gas reservoir. Interferometric imaging of the ^{13}CO (1–0) and (2–1) lines in the literature reveal a gaseous disk structure of 600 AU in extent (Kitamura et al. 1996a,b; Testi et al. 2002), about 4–6 times the size inferred from dust emission. Accordingly, we adopt 600 AU for the outer radius of the gas disk, extrapolating the initial Robitaille model outwards. In addition, the ^{13}CO (2–1) emission observed by Testi et al. (2002) is
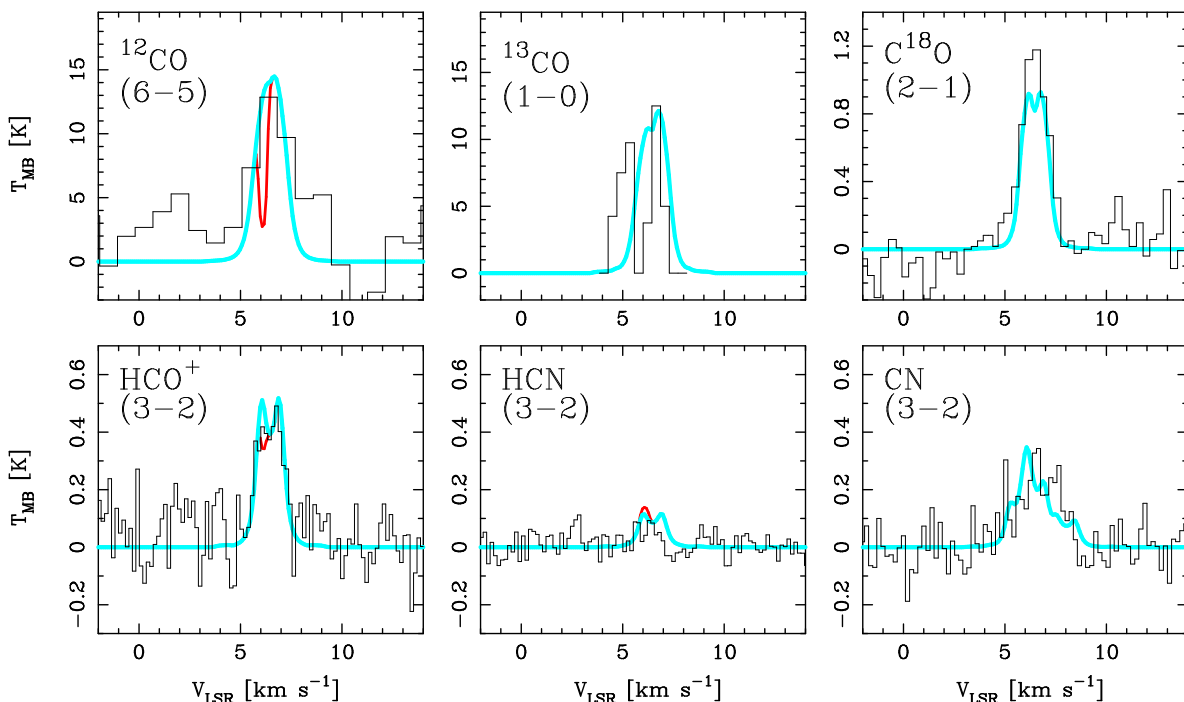
Figure 2.10 — Line predictions for our best-fitting model of DG Tau. The ^{12}CO (6–5) and C^{18}O (2–1) data are taken from Schuster et al. (1993) where their T_R^* scale is equivalent to our T_{mb} scale. The ^{13}CO (1–0) is from Kitamura et al. (1996a), and since we were unable to establish a conversion from Jy to K, we compare the *line shape* only. We have indicated with a thick blue line our fits for a 600 AU disk at an inclination of 25°. Indicated in red is how the (^{12}CO, HCO$^+$, and HCN) line profiles are affected by the absorption or excess emission from a cold, foreground cloud at a radial velocity of 6.1 km s^{-1}. No differences are visible for the ^{13}CO or C^{18}O lines. The effect of the foreground cloud on the CN line is not available; but the expected hyperfine line-splitting is calculated.

consistent with Keplerian rotation around a star of $0.67 \pm 0.25 \, M_\odot$, oriented perpendicular (within $\pm 15°$) to the highly collimated jet system, which is inclined 38° with respect to the line of sight (Eislöffel & Mundt 1998). Therefore, we adopt an inclination of 25°, which also gives the best fit to the C^{18}O (2–1) line profile. We already show in Figure 2.10—and we will discuss later in this section—the minimal effect from intervening cloud or remnant envelope material in this line.

With the stellar mass ($M_\star = 0.8 \, M_\odot$), inclination ($i = 25°$), and outer gas radius ($R_d = 600$ AU) now fixed, we use a constant fractional CO abundance of 2×10^{-4} and C^{18}O abundance of 4×10^{-7} (except when $T < 20$ K, where an abundance 10^3 times lower is used) to calculate the simulated line profiles with RATRAN using the extended and modified Robitaille model. To fit the lines, particularly C^{18}O, we find that we need to increase the gas temperature by a factor 1.7; suggesting that the line emission originates in layers where $T_{gas} > T_{dust}$. We adopt this same scaling for the gas temperature for all species, but neglect its effect on the scale height.

For these model parameters, the HCO$^+$ line can be very well reproduced for a disk-averaged abundance of 2×10^{-11} with respect to H$_2$. This is lower than theoretical predictions for the warm emission layer in many T Tauri disks (Aikawa et al. 2002; van Zadelhoff et al. 2003), but not unlike the beam-averaged fractional abundances ($\sim 10^{-11}$–10^{-12}) inferred from observations of disks around several high-mass (Herbig Ae/Be) stars (see Thi et al. 2004). A low mean abundace is also especially surprising given DG Tau's powerful jets emit significant X-ray radiation (Güdel et al. 2008). Apparently, the disk is sufficiently shielded to retain a low ionization degree. An upper limit for the HCN abundance

of 5×10^{-12} is found, while a value of 8×10^{-10} is obtained for CN. This high CN/HCN ratio of > 160 suggests efficient HCN dissociation in the bulk of the disk, which is more consistent with its mid-infrared characterization indicating fewer small grains and some dust settling. Here we note the importance of using *abundance* ratios rather than line *intensity* ratios (which contain opacity and excitation effects): the ratio of integrated intensities of CN/HCN used in Section 2.3 is > 12, a factor of 13 smaller than the underlying abundance ratio found here.

The disk abundances above have been derived using the density and temperature structure of the best-fitting Robitaille model, with noted modifications. The results are summarized in Table 2.7. Substituting the description of Isella instead, but applying the same values for $M_\star$ and i, and the emergent line intensities are lower by up to a factor of ~ 16 for HCO$^+$ for the same abundances, and by smaller factors of ~ 5 and ~ 10 for HCN and CN, respectively. The large line intensity differences result also from the differences in $R_{\rm gas}$ for each model. Whereas the Robitaille power-law model for the temperature and density description (and sharp outer dust edge) leads easily to extrapolation to larger radii, the Isella model, with its exponentially tapered density structure, does not. Thus, to compare the two disk structures in a uniform way, we plot the temperature and density profiles for each model for the *inner* 160 AU *only* in Figure 2.11. Then, in Figure 2.12 we plot the predicted lines. Unlike Figures 2.8 and 2.9, we now assume identical gas kinematic properties ($M_\star$, i, and $R_{\rm gas}$). The predicted lines for each model in Figure 2.12 are now strikingly similar. The differences in the two emerging line intensities are lower by up to a factor of 2 for HCO$^+$ and much closer for HCN and CN. This suggests that the large CN/HCN ratio of > 160 found for the underlying abundances is independent of the temperature and density details of the adopted model (for the inner 160 AU); and leaves only the missing details of the input radiation field uninvestigated.

Table 2.6 — DG Tau star and disk properties from the literature to compare with the two disk models.

Property	Isella Model	Robitaille Model	Literature Range	References
Spectral Type	M0	-	K1–K7	2, 10, 12, 23
$M_\star$ [$M_\odot$]	0.3	1.48	0.3–0.8	4, 5, 17, 20
Age [Myr]	0.1	1.89	0.3–2.0	5, 11, 13
$T_{\rm eff}$ [K]	3890	4560	3890–4395	5, 7, 11, 17
$L_\star$ [$L_\odot$]	1.70	-	1.07–3.62	1, 4, 5, 18
$R_\star$ [$R_\odot$]	2.87	2.427	2.13–2.8	3, 11, 17
$\dot{M}$ [$M_\odot\,{\rm yr}^{-1}$]	4.1e^{-7}	4.5e^{-7}	1.2–20e^{-7}	11, 17, 18
$M_{\rm d}$ [$10^{-2}\,M_\odot$]	41.7	3.9	1.5–2.51	2, 6, 9, 13
$R_{\rm dust}$ [AU]	89	158	80–300	9, 16, 19
$R_{\rm gas}$ [AU]	160	600	600	16, 24
i [°]	18	25	18-90	3, 9, 14, 16
$A_{\rm v}$ [mag]	-	1.6	1.41–1.6	10, 22
Dist. [pc]	140	140	128–156	10, 21

References. (1) Akeson et al. (2005); (2) Andrews & Williams (2005); (3) Appenzeller et al. (2005); (4) Basri et al. (1991); (5) Beckwith et al. (1990); (6) Beckwith & Sargent (1991); (7) Bouvier et al. (1995); (8) Cieza et al. (2005); (9) Dutrey et al. (1996); (10) Furlan et al. (2006); (11) Hartigan et al. (1995); (12) Hessman & Guenther (1997); (13) Honda et al. (2006); (14) Isella et al. (2009); (15) Kenyon & Hartmann (1995); (16) Kitamura et al. (1996b); (17) Mohanty et al. (2005); (18) Muzerolle et al. (2003); (19) Rodmann et al. (2006); (20) Tamura et al. (1999); (21) Vinković & Jurkić (2007); (22) White & Ghez (2001); (23) White & Hillenbrand (2004); and (24) Testi et al. (2003).

Table 2.7 — Determined abundances for our best-fit DG Tau model.

Molecule	DG Tau	Theoretical
Disk Fractional Abundances (w.r.t. H_2)[a]		
^{12}CO	2.0×10^{-4}	1.0×10^{-4}
^{13}CO	3.3×10^{-6}	1.7×10^{-6}
$C^{18}O$	4.0×10^{-7}	2.0×10^{-7}
HCO^+	2.0×10^{-11}	1–100×10^{-11}
HCN	5.0×10^{-12}	1–100×10^{-11}
CN	8.0×10^{-10}	1–100×10^{-11}
Cloud Fractional Abundances (w.r.t. H_2)[b]		
^{12}CO	2.0×10^{-4}	8.0×10^{-5}
^{13}CO	3.3×10^{-6}	-
$C^{18}O$	4.0×10^{-7}	-
HCO^+	8.0×10^{-9}	8.0×10^{-9}
HCN	8.0×10^{-9}	4–20×10^{-9}
CN[c]	-	3–30×10^{-9}
Cloud Column Densities (cm^{-2})		
^{12}CO	6.0×10^{16}	$\cdots$
^{13}CO	1.0×10^{15}	$\cdots$
$C^{18}O$	1.2×10^{14}	$\cdots$
HCO^+	2.4×10^{12}	$\cdots$
HCN	2.4×10^{12}	$\cdots$
CN	-	$\cdots$

Notes. (a) The DG Tau abundances are constant throughout the disk (or disk-averaged), whereas the theoretical disk abundances from Aikawa et al. (2002) and van Zadelhoff et al. (2003) represent the ranges expected in the warm molecular layers only; (b) The theoretical cloud values are from Terzieva & Herbst (1998); (c) The online RADEX program does not yet include CN (to calculate the cloud contributions).

Finally, DG Tau is not an isolated source. The environment around the star is dominated by an optical jet (Eislöffel & Mundt 1998), a strong molecular outflow (Mitchell et al. 1994), an expanding circumstellar envelope (Kitamura et al. 1996b), and intervening cloud material (this work). The result of this confused environment is most clearly evident when comparing the ^{12}CO (3–2) line observations presented in Schuster et al. (1993) and Mitchell et al. (1994), which exhibit equally bright line intensities and significant wings at the on-source position and three separate offset positions. We chose to omit the ^{12}CO observations from the fits in Figure 2.10, since they distract from the disk emission. However, we do determine that the ^{12}CO lines are about $3\times$ stronger than predicted for our disk model, suggesting contributions from a surrounding cloud with a CO column density of $N_{CO} \approx 6 \times 10^{16}\,cm^{-2}$ and line width of $0.3\,km\,s^{-1}$ for an adopted cloud temperature of $25\,K$ and H_2 number density of $10^4\,cm^{-3}$ (or $N_{CO} \approx 1 \times 10^{16}\,cm^{-2}$ for an H_2 number density of $10^5\,cm^{-3}$). For these typical cloud densities, we do not expect significant HCO^+ (3–2), HCN (3–2), or CN (2–1) emission (or absorption); and both Figures 2.4 and 2.10 confirm this.

To determine those line contributions from the cloud, plotted in Figure 2.10, as well as the cloud fractional abundances and column densities listed in Table 2.7, we used the RADEX[5] online calculator. We

---

[5]RADEX is an online, one-dimensional, non-LTE radiative transfer code developed by (van der Tak et al. 2007) to calculate the molecular line intensity, opacity, and excitation temperature. For more information, see http://www.sron.rug.nl/~vdtak/radex/radex.php
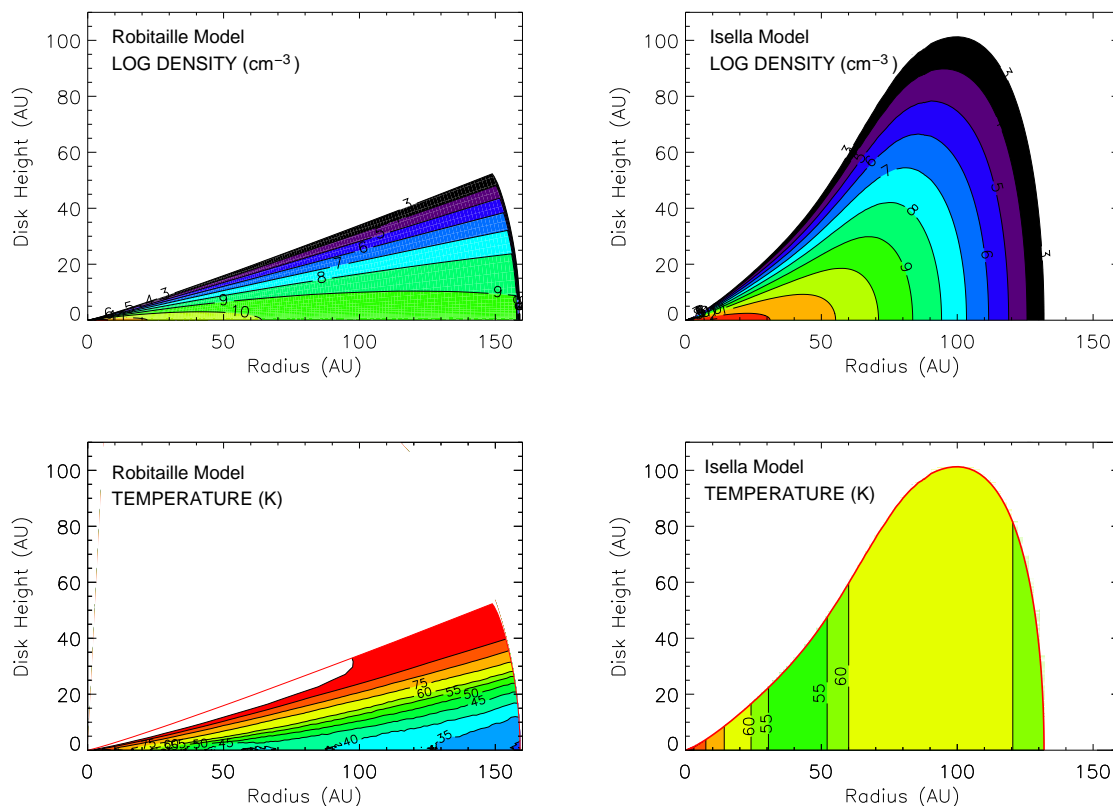
Figure 2.11 — The radial and vertical structures for the *inner* 160 AU of each disk model, for direct comparison. The panels at left show the Robitaille model (without the extended gas reservoir), and the panels at right show the full Isella model (with exponential taper). The upper panels indicate the temperature structures, and the lower panels compare the density structures for each model.

modeled the cloud as a cold intervening layer moving with a radial velocity of $6.1 \, \mathrm{km \, s^{-1}}$. We note that in many of the literature observations, strong absorption is seen near a velocity of 5.8–$6.2 \, \mathrm{km \, s^{-1}}$, with several studies reporting these values as the source velocity. We emphasize here that our observations of HCO⁺, with a critical density 3 orders of magnitudes larger than the CO observations in the literature, are a much better tracer of the disk content, establishing the source radial velocity at $6.47 \, \mathrm{km \, s^{-1}}$. In addition, we confirm that the emerging HCO⁺ line predicted for our intervening cloud fits the detections observed at both DG Tau offset positions ($\sim$0.25 K peak centered at $6.1 \, \mathrm{km \, s^{-1}}$, see Figure 2.4). The effect of the intervening material on the observed ^{12}CO, HCO⁺, and HCN lines is shown in Figure 2.10, while ^{13}CO and C^{18}O exhibit no differences, and the CN cloud predictions are not yet available in the RADEX program.

2.5.4   Notes on Individual Sources

V806 Tau, also called Haro 6–13, has the second strongest HCO⁺ line after DG Tau, but is undetected in HCN and CN. It is a single M0 star. With an $A_v = 11.2$, its optical extinction is much larger than our other sources, which might help explain its unique silicate emission feature and positive spectral slope. Furlan et al. (2006) comment that the silicate features are reminiscent of transitional disks, although it also possesses a high mass accretion rate (White & Hillenbrand 2004). Some extended HCO⁺ emission is apparent in Figure 2.4. However, our single-dish radial velocity of $5.40 \, \mathrm{km \, s^{-1}}$ is consistent with the
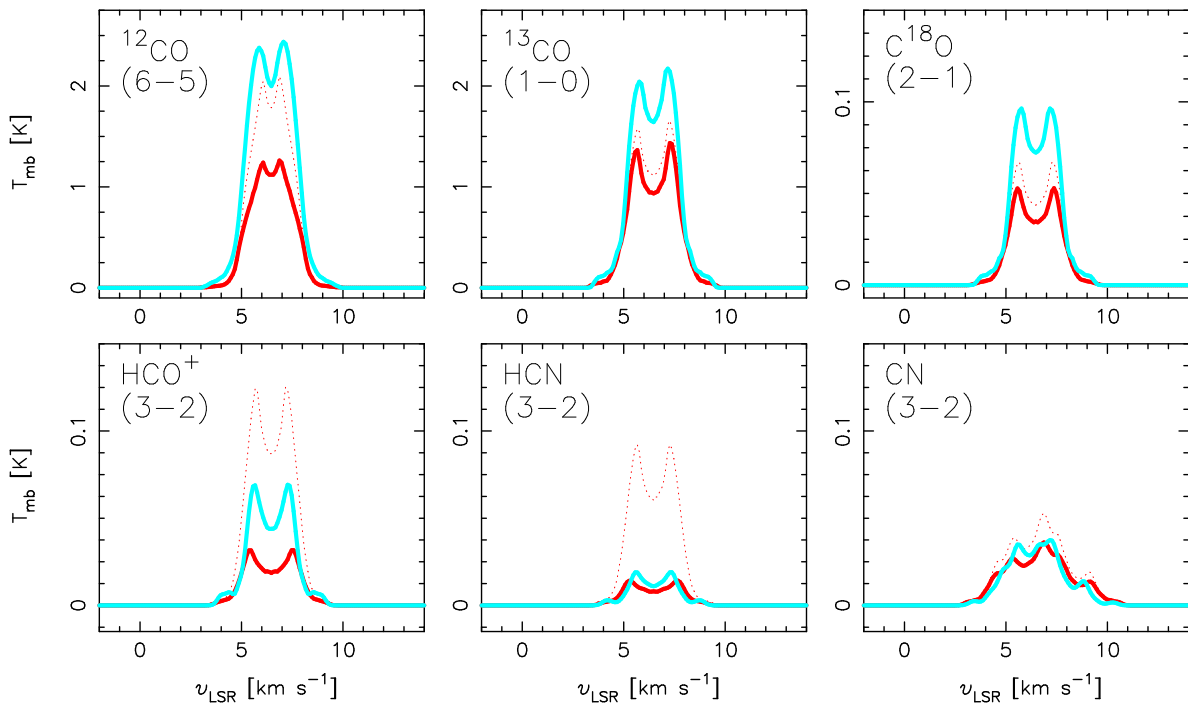
Figure 2.12 — Similar to Figures 2.8 and 2.9, the line predictions for the two models for the *inner* 160 AU, assuming identical abundances, T_{kin}, $M_{\star}$, and i, in order to uniformly compare the predicted emission. A solid blue line represents the Robitaille solution, whilst a red line is the Isella prediction. The corresponding temperature and density structures are given in Figure 2.11. In addition, as a dashed red line, we plot the most extreme solution to the Isella model, based on the provided error bars and the largest possible fractional abundances predicted for disks. For both models, the inner 160 AU structure emits only a small fraction of the total emission necessary to recreate the observed lines, but the two predictions are very similar.

value of $5.10 \, \text{km s}^{-1}$ from CO interferometric observations (Schaefer et al. 2009). V806 Tau's low disk mass of $0.01 \, M_{\odot}$ (Andrews & Williams 2005; Honda et al. 2006) and large 400 AU radius (Robitaille et al. 2006) suggest that much of the disk of V806 Tau should be UV illuminated, in contrast to our observed upper limit for CN.

GO Tau shows complex line profiles, with peaks at a v_{LSR} of 4.4, 5.1, 5.5, and 6.3 km s^{-1}. Thi et al. (2001) report ^{12}CO emission peaks at 5.2, 5.5, 6.2, and 7.1 km s^{-1}, and ^{13}CO emission at 4.3 and 7.0 km s^{-1}. They attribute the 5.5 and 6.2 km s^{-1} components to surrounding cloud emission. However, we assign the emission between 4–6 km s^{-1} to the disk of GO Tau, as suggested by the interferometric observations of Schaefer et al. (2009) and Andrews (2007). For GO Tau, the accretion rate is very low (Hartmann et al. 1998), and the amount of dust settling is small if we draw on its mid-infrared spectral slope, suggesting lower rates of UV photodissociation and ionization should be occurring. However, it exhibits one of the brightest HCO^{+} lines, in stark contrast to the rest of the sample since its fainter 1.3 mm continuum flux just straddles our cutoff and yet the source also appears to be associated with a large, and dense, gas reservoir.

DR Tau also has a complicated circumstellar environment, with ^{12}CO emission lines at 6.8, 9.1, 10.0, and 10.3 km s^{-1} and ^{13}CO emission at 6.9 km s^{-1} and near 11 km s^{-1} (Thi et al. 2001). SMA interferometric observations by Andrews (2007) also show strong emission centered on 10.5 km s^{-1}, suggesting that this is the correct source velocity. Our CN spectrum shows a triple-peaked 5.4σ feature centered at 11.2 km s^{-1} (Figure 2.3). Our model results suggest that 'standard' HCO^{+} and HCN abundances are consistent with the non-detections of the lines. The CN detection in the absence of the other lines, on the

other hand, indicates a significant CN enhancement.

CW Tau is clearly surrounded by dense cloud material, as witnessed by the eqally strong HCO$^+$ emission on- and off-source. Our HCO$^+$ observations (see Figure 2.4) illustrate how, in a crowded star-forming region, measurements at offset positions can be both relevant and useful even for molecular species that preferentially trace much denser material.

CY Tau, DQ Tau, IQ Tau, and **UZ Tau** do not show gas emission lines in our data. Interestingly, they span the full dust classification and morphological sequence of Furlan et al. (2006) with CY Tau and DQ Tau showing rather flat, decreasing mid-infrared SEDs, and IQ Tau and UZ Tau showing evidence for a small grain population. The mass accretion rates – which contribute to the stellar UV excess – range from very low ($10^{-9}\,M_\odot\,\mathrm{yr}^{-1}$) for CY Tau to average ($10^{-7}\,M_\odot\,\mathrm{yr}^{-1}$) for DQ Tau and UZ Tau (Güdel et al. 2007). However, both DQ Tau and UZ Tau E are spectroscopic binaries that exhibit pulsed accretion events on periods of weeks (Basri et al. 1997), and their higher reported accretion rates may overestimate the average, quiescent values.

2.6   Discussion

To return to previous work, Kastner et al. (2008b) showed plots of HCO$^+$, HCN, and CN line ratios for several PMS stars, showing a tentative correlation between the HCO$^+$, HCN, CN, and ^{13}CO line ratios. In Figure 2.13 we reproduce their plots and their data points (without error bars), and add our own line ratios. Overall, we find that the trends persist: CN is typically stronger than HCN, CN is also stronger than HCO$^+$, and the photodissociation rate (as probed by CN/HCN) is roughly constant regardless of the HCN relative line strength. Our contributed line ratios consist largely of upper and lower limits and therefore do not specifically challenge or confirm the trends by probing different regions in the plots. While this complete PMS sample in Figure 2.13 includes sources covering a range in age, mass, and radiation field, the line strengths of HCO$^+$, HCN, and CN relative to one another do reveal the importance of the ongoing UV photodissociation and X-ray ionization processes in these disks. The results, however, are still limited by small numbers statistics, numerous upper limits, and different rotational transitions (that may trace different regions of the disk).

The motivation of this study was to determine whether disks with a higher degree of dust settling, or with a decreased dust content, have higher abundances of CN and HCO$^+$ reflecting larger degrees of photodissociation and photoionization. Our data are inconclusive. In Section 2.4 we found that the HCO$^+$, HCN, and CN line fluxes (or their ratios) do not depend on any other disk or stellar parameter such as millimeter flux, infrared slope, silicate feature strength, stellar spectral type, etc. Section 2.5 shows that detailed SED-based models have intrinsic degeneracies that preclude straight-forward modeling. And even a detailed model, tailored to the case of DG Tau, does not provide unambiguous estimates of the HCO$^+$, HCN, and CN abundances.

This suggests two possible ways forward. In the first, spatially resolved observations of both the dust continuum and the line emission can be used to obtain *in situ* measurements of the molecular abundances. ALMA will be a powerful instrument for an analysis like this. By addressing localized disk regions, rather than the emission integrated over the entire face of the disk, more simplified modeling approaches can be used (not unlike what is presently state-of-the-art analyses for photon dominated regions, PDRs). In addition, spatially resolved observations provide many more constraints on the underlying disk structure, such as the extent and surface density. This approach addresses the question of how molecular line emission and underlying disk structure are interrelated.

The second approach does not focus on the details of the underlying disk structure, but rather the details of the star's radiation field, which irradiates the disk. Accurate determination of the spectral type and luminosity, the UV and X-ray emission characteristics, and their time dependences should lead to a better
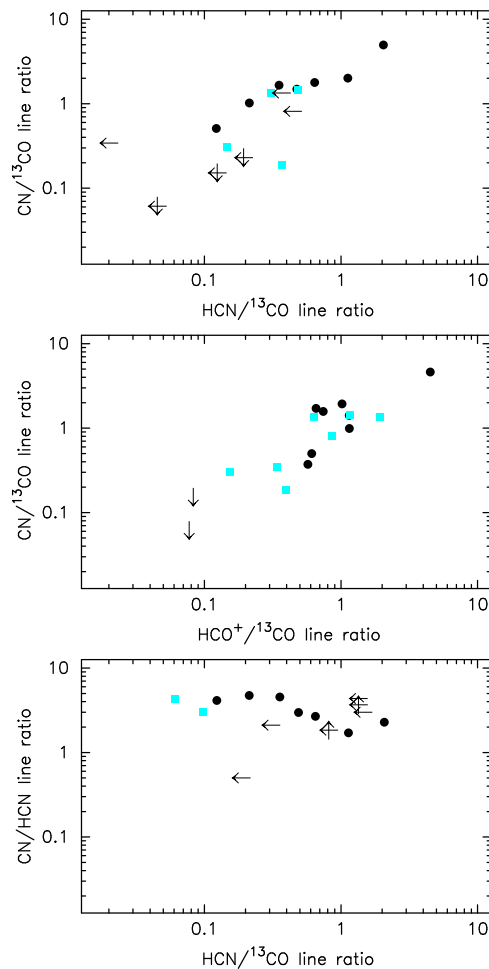
Figure 2.13 — Integrated intensity line ratios for HCO$^+$, HCN, CN, and ^{13}CO plotted alongside other disk systems around PMS stars in the literature. Circles represent data points extracted from Figure 3 of (Kastner et al. 2008b), squares represent data points from our complete Taurus sample, and black arrows represent upper/lower limits.

understanding of the *response* of the molecular gas reservoir to the incident radiation. High-resolution, high signal-to-noise observations are time-consuming but necessary for better stellar characterization of PMS stars, while veiling and other circumstellar environmental effects provide challenges that have been overcome (Merín et al. 2004; Herczeg & Hillenbrand 2008). Recent studies have even argued that the continuum UV spectrum for T Tauri stars must be much weaker, due to the total fraction of the stellar FUV flux that is emitted in the Lyα line alone. Since this fraction can range from 30% up to 85% (for TW Hya), Lyα provides an additional source of photodissociating power that varies from source-to-source and is extremely difficult to measure (Bergin et al. 2003). Which of these two approaches is most fruitful will, of course, depend on which factor dominates the molecular line emission: the underlying disk structure or the stellar irradiation. Since these may be interrelated, both approaches may prove necessary.

2.7 Summary

We surveyed 13 classical T Tauri stars in low-*J* transitions of HCO$^+$, HCN, and CN to compare the gas structure and chemical abundances within planet-forming disks that possess similar dust masses. We found, conversely, a wide variety of molecular gas properties. For this sample in the Taurus star-forming

region, we report 6 new disk detections of HCO$^+$ (3–2), 0 new detections of HCN (3–2), and 4 new detections of CN ($J = 2$–1). These data double the pool of previously known detections, bringing the total detection statistics for the 21 brightest (at 1.3 mm) disks in Taurus to: 14 for HCO$^+$, 5 for HCN, and 8 for CN.

Overall the HCO$^+$, HCN, and CN line ratios for our Taurus disk sample are consistent with the trends identified toward other disks around PMS stars found in the literature, as initially plotted by Kastner et al. (2008a,b). In general, CN is more prevalent than HCN, which suggests that the bulk of the detected emission originates in a UV photodissociating region. Additionally, the fractional molecular ionization ratio, as traced in only slightly denser regions by the HCO$^+$ line, is also enhanced. Both trends agree with the narrow emission lines observed in our sample, which trace the outermost regions where the disk is optically thin to *both* the stellar and interstellar radiation fields.

Despite this disk-to-disk agreement in the line ratios toward the general population of unresolved disks, the gas-line properties reveal *no* observed chemical photoprocessing effects due to the dust properties or several stellar parameters, which was the main motivation for this research. We do not see CN and HCO$^+$ enhancements (via brighter lines) in sources whose mid-infrared spectral slope and silicate emission features indicate more grain growth and dust settling (leading to a lack of UV shielding). In addition, stellar parameters like X-ray luminosity do not seem to influence the observed line intensities of ionization tracers such as HCO$^+$.

The next step was to derive the underlying molecular abundances using two dust models in the literature that are then populated with theoretical values for the fractional molecular abundances. Models for the sample as a whole illustrate the importance of the $M_\star \sin i$ and R_{gas} factors in gas-line abundance studies; parameters that are poorly constrained by the dust properties, but critical to proper line fits. Along these lines, we found during detailed modeling of the source DG Tau that the underlying abundances were less dependent of the temperature and density details in the adopted dust models. We conclude that better characterization of the stellar parameters ($M_\star$), the radiation field itself (UV and Lyα), and spatially-resolved line observations (R_{gas} and i) are necessary to constrain the molecular gas content and evolution.

Large sample statistics are still a challenge. It remains a future task for ALMA, with its the resolution and sensitivity advancements, to resolve these disks (including inner and outer disk differences), their gaseous surface density profiles, and the chemical signatures of changes in the inner dust structure. Only then will we be able to examine how photodissociation, ionization, and freeze-out processes affect the surface density of the gas by comparison to resolved dust observations.

Acknowledgements

Bibliography

Aikawa, Y., van Zadelhoff, G. J., van Dishoeck, E. F., & Herbst, E. 2002, A&A, 386, 622
Akeson, R. L., Boden, A. F., Monnier, J. D., et al. 2005, ApJ, 635, 1173
Andrews, S. M. 2007, PhD thesis, University of Hawai'i at Manoa
Andrews, S. M. & Williams, J. P. 2005, ApJ, 631, 1134
Appenzeller, I., Bertout, C., & Stahl, O. 2005, A&A, 434, 1005
Basri, G., Johns-Krull, C. M., & Mathieu, R. D. 1997, AJ, 114, 781

Basri, G., Martin, E. L., & Bertout, C. 1991, A&A, 252, 625

Beckwith, S. V. W. 1996, Nature, 383, 139

Beckwith, S. V. W. & Sargent, A. I. 1991, ApJ, 381, 250

Beckwith, S. V. W., Sargent, A. I., Chini, R. S., & Guesten, R. 1990, AJ, 99, 924

Bergin, E., Calvet, N., D'Alessio, P., & Herczeg, G. J. 2003, ApJ, 591, L159

Bouvier, J., Covino, E., Kovo, O., et al. 1995, A&A, 299, 89

Calvet, N., D'Alessio, P., Hartmann, L., et al. 2002, ApJ, 568, 1008

Chapillon, E., Guilloteau, S., Dutrey, A., & Piétu, V. 2008, A&A, 488, 565

Chiang, E. I. & Goldreich, P. 1997, ApJ, 490, 368

Cieza, L. A., Kessler-Silacci, J. E., Jaffe, D. T., Harvey, P. M., & Evans, II, N. J. 2005, ApJ, 635, 422

Damiani, F., Micela, G., Sciortino, S., & Harnden, Jr., F. R. 1995, ApJ, 446, 331

Dullemond, C. P. & Dominik, C. 2004, A&A, 421, 1075

Dutrey, A., Guilloteau, S., Duvert, G., et al. 1996, A&A, 309, 493

Dutrey, A., Guilloteau, S., & Guelin, M. 1997, A&A, 317, L55

Dutrey, A., Guilloteau, S., & Ho, P. 2007, in Protostars and Planets V, ed. B. Reipurth, D. Jewitt, & K. Keil, 495–506

Eislöffel, J. & Mundt, R. 1998, AJ, 115, 1554

Fuente, A., Martin-Pintado, J., Cernicharo, J., & Bachiller, R. 1993, A&A, 276, 473

Furlan, E., Hartmann, L., Calvet, N., et al. 2006, ApJS, 165, 568

Glassgold, A. E., Najita, J., & Igea, J. 2004, ApJ, 615, 972

Greaves, J. S. 2004, MNRAS, 351, L99

Greaves, J. S. 2005, MNRAS, 364, L47

Greaves, J. S. & Church, S. E. 1996, MNRAS, 283, 1179

Güdel, M. 2008, Astronomische Nachrichten, 329, 218

Güdel, M., Briggs, K. R., Arzner, K., et al. 2007, A&A, 468, 353

Güdel, M., Skinner, S. L., Audard, M., Briggs, K. R., & Cabrit, S. 2008, A&A, 478, 797

Guilloteau, S., Dutrey, A., & Simon, M. 1999, A&A, 348, 570

Hartigan, P., Edwards, S., & Ghandour, L. 1995, ApJ, 452, 736

Hartmann, L., Calvet, N., Gullbring, E., & D'Alessio, P. 1998, ApJ, 495, 385

Herbig, G. H. & Bell, K. R. 1988, Third Catalog of Emission-Line Stars of the Orion Population : 3 : 1988, ed. Herbig, G. H. & Bell, K. R.

Herbig, G. H. & Goodrich, R. W. 1986, ApJ, 309, 294

Herczeg, G. J. & Hillenbrand, L. A. 2008, ApJ, 681, 594

Hessman, F. V. & Guenther, E. W. 1997, A&A, 321, 497

Hogerheijde, M. R., Jansen, D. J., & van Dishoeck, E. F. 1995, A&A, 294, 792

Hogerheijde, M. R. & Sandell, G. 2000, ApJ, 534, 880

Hogerheijde, M. R. & van der Tak, F. F. S. 2000, A&A, 362, 697

Hogerheijde, M. R., van Dishoeck, E. F., Blake, G. A., & van Langevelde, H. J. 1998, ApJ, 502, 315

Honda, M., Kataza, H., Okamoto, Y. K., et al. 2006, ApJ, 646, 1024

Hughes, A. M., Wilner, D. J., Qi, C., & Hogerheijde, M. R. 2008, ApJ, 678, 1119

Isella, A., Carpenter, J. M., & Sargent, A. I. 2009, ApJ, 701, 260

Jørgensen, J. K., Schöier, F. L., & van Dishoeck, E. F. 2004, A&A, 416, 603

Kastner, J. H., Zuckerman, B., & Forveille, T. 2008a, A&A, 486, 239

Kastner, J. H., Zuckerman, B., Hily-Blant, P., & Forveille, T. 2008b, A&A, 492, 469

Kastner, J. H., Zuckerman, B., Weintraub, D. A., & Forveille, T. 1997, Science, 277, 67

Kenyon, S. J., Dobrzycka, D., & Hartmann, L. 1994, AJ, 108, 1872

Kenyon, S. J. & Hartmann, L. 1995, ApJS, 101, 117

Kessler-Silacci, J. 2004, PhD thesis, AA(CALIFORNIA INSTITUTE OF TECHNOLOGY)

Kitamura, Y., Kawabe, R., & Saito, M. 1996a, ApJ, 457, 277

Kitamura, Y., Kawabe, R., & Saito, M. 1996b, ApJ, 465, L137+

Koerner, D. W. & Sargent, A. I. 1995, AJ, 109, 2138

Lepp, S. & Dalgarno, A. 1996, A&A, 306, L21

Luhman, K. L., Allen, P. R., Espaillat, C., Hartmann, L., & Calvet, N. 2010, ApJS, 186, 111

Mannings, V. & Sargent, A. I. 1997, ApJ, 490, 792

Mannings, V. & Sargent, A. I. 2000, ApJ, 529, 391

Merín, B., Montesinos, B., Eiroa, C., et al. 2004, A&A, 419, 301

Mitchell, G. F., Hasegawa, T. I., Dent, W. R. F., & Matthews, H. E. 1994, ApJ, 436, L177

Mohanty, S., Jayawardhana, R., & Basri, G. 2005, ApJ, 626, 498

Muzerolle, J., Calvet, N., Hartmann, L., & D'Alessio, P. 2003, ApJ, 597, L149

Natta, A., Testi, L., Calvet, N., et al. 2007, Protostars and Planets V, 767

Palla, F. & Stahler, S. W. 2002, ApJ, 581, 1194

Panić, O., Hogerheijde, M. R., Wilner, D., & Qi, C. 2008, A&A, 491, 219

Piétu, V., Dutrey, A., & Guilloteau, S. 2007, A&A, 467, 163

Rebull, L. M., Padgett, D. L., McCabe, C., et al. 2010, ApJS, 186, 259

Robitaille, T. P., Whitney, B. A., Indebetouw, R., & Wood, K. 2007, ApJS, 169, 328

Robitaille, T. P., Whitney, B. A., Indebetouw, R., Wood, K., & Denzmore, P. 2006, ApJS, 167, 256

Rodmann, J., Henning, T., Chandler, C. J., Mundy, L. G., & Wilner, D. J. 2006, A&A, 446, 211

Schaefer, G. H., Dutrey, A., Guilloteau, S., Simon, M., & White, R. J. 2009, ApJ, 701, 698

Schreyer, K., Guilloteau, S., Semenov, D., et al. 2008, A&A, 491, 821

Schuster, K. F., Harris, A. I., Anderson, N., & Russell, A. P. G. 1993, ApJ, 412, L67

Simon, M., Dutrey, A., & Guilloteau, S. 2000, ApJ, 545, 1034

Tamura, M., Hough, J. H., Greaves, J. S., et al. 1999, ApJ, 525, 832

Terzieva, R. & Herbst, E. 1998, ApJ, 501, 207

Testi, L., Bacciotti, F., Sargent, A. I., Ray, T. P., & Eislöffel, J. 2002, A&A, 394, L31

Testi, L., Natta, A., Shepherd, D. S., & Wilner, D. J. 2003, A&A, 403, 323

Thi, W., van Zadelhoff, G., & van Dishoeck, E. F. 2004, A&A, 425, 955

Thi, W. F., van Dishoeck, E. F., Blake, G. A., et al. 2001, ApJ, 561, 1074

van der Tak, F. F. S., Black, J. H., Schöier, F. L., Jansen, D. J., & van Dishoeck, E. F. 2007, A&A, 468, 627

van Kempen, T. A., van Dishoeck, E. F., Brinch, C., & Hogerheijde, M. R. 2007, A&A, 461, 983

van Zadelhoff, G.-J., Aikawa, Y., Hogerheijde, M. R., & van Dishoeck, E. F. 2003, A&A, 397, 789

Vinković, D. & Jurkić, T. 2007, ApJ, 658, 462

Weidenschilling, S. J. 1997, Icarus, 127, 290

White, R. J. & Ghez, A. M. 2001, ApJ, 556, 265

White, R. J. & Hillenbrand, L. A. 2004, ApJ, 616, 998

Whitney, B. A., Wood, K., Bjorkman, J. E., & Wolff, M. J. 2003, ApJ, 591, 1049

Yun, J. L., Moreira, M. C., Afonso, J. M., & Clemens, D. P. 1999, AJ, 118, 990